Multinucleon transfer mechanism in ^{160}Gd + ^{186}W collisions in stochastic mean-field theory

S. Ayik [1,*] M. Arik [2] E. Erbayri [2] O. Yilmaz [2] and A. S. Umar [3]
[1]*Physics Department, Tennessee Technological University, Cookeville, Tennessee 38505, USA*
[2]*Physics Department, Middle East Technical University, 06800 Ankara, Turkey*
[3]*Department of Physics and Astronomy, Vanderbilt University, Nashville, Tennessee 37235, USA*

(Received 27 July 2023; accepted 12 October 2023; published 20 November 2023)

The multinucleon transfer mechanism in ^{160}Gd + ^{186}W collisions is investigated in the framework of quantal transport description, based on the stochastic mean-field (SMF) theory. The SMF theory provides a microscopic approach for nuclear dynamics beyond the time-dependent Hartree-Fock approach by including mean-field fluctuations. Cross sections for the primary fragment production are determined in the quantal transport description and compared with the available data.

DOI: 10.1103/PhysRevC.108.054605

I. INTRODUCTION

The production of heavy elements near the superheavy island with proton numbers $Z > 100$ embodies one of the greatest experimental and theoretical challenges [1–16]. The most common approach for the production of these elements and their isotopes is through fusion reactions. Historically, two distinct experimental approaches have been employed to synthesize these nuclei, named, based on their excitation properties, as cold fusion reactions [17] and hot fusion reactions [14,18]. The primary composite systems formed in these reactions are at a relatively high excitation energy, which subsequently deexcites by emitting neutrons, α particles, and secondary fission. This results in exceedingly small evaporation residue cross sections, which makes reaching heavier elements as well as the neutron rich isotopes of these elements very difficult. To circumvent this obstacle, multinucleon transfer reactions have been proposed as an alternative. Such experiments have recently focused on using actinide targets at near the Coulomb barrier energies. Using this approach, it is possible to produce heavy primary fragments at reasonably lower excitation energies. Consequently, such reactions may provide a more efficient mechanism for the production of heavy neutron-rich isotopes than fusion, fission, and fragmentation reactions. In collisions involving deformed target nuclei, multinucleon transfer depends on the collision geometry. In a typical collision, the system drifts toward symmetry. However, for certain geometries the system may drift toward asymmetry, which is referred to as inverse quasifission. The multinucleon transfer mechanism has been studied by employing a number of phenomenological approaches, such as the multidimensional Langevin model [19–25], the dinuclear system model [26–28], and the quantum molecular dynamics approach [29–31].

To formulate a reliable description of the multiparticle transfer mechanism and its dependence on the collision geometry it is essential to utilize microscopic approaches. Time-dependent Hartree-Fock (TDHF) theory is a good candidate as the basis for such a microscopic description to describe the evolution of collective dynamics at low bombarding energies [32–41]. Despite its success, TDHF theory, based on the mean-field approach, only describes the most probable path of the collision dynamics with small fluctuations around it. By virtue of this limitation TDHF theory generally describes the mean values of observables, such as the kinetic energy loss involving one-body dissipation, but is unable to account for larger fluctuations and dispersions of the fragment mass and charge distributions. In order to account for these observables it is necessary to find a prescription that goes beyond the mean-field approximation [42–48]. One such approach is through the time-dependent random-phase approximation (TDRPA) developed by Balian and Véneroni, which provides a consistent theory to compute larger fluctuations of the observables going beyond mean field. This method has been used to study multinucleon transfer reactions in symmetric systems [49–52], and it is inherently constrained to compute the dispersion of charge and mass distributions in symmetric collisions.

The stochastic mean-field (SMF) theory, closely related to the TDRPA, circumvents this problem and facilitates further improvements to the beyond-mean-field approximation [47,48]. The paper is organized as follows. In Sec. II, we provide results of TDHF calculations for the collisions of the ^{160}Gd + ^{186}W system at $E_{\rm c.m.} = 502.6$ MeV and $E_{\rm c.m.} = 461.9$ MeV. Section III briefly describes multinucleon transfer as constituted in the quantal transport description of the SMF approach. In this reaction both projectile and target nuclei are two deformed isotopes between doubly closed ^{132}Sn and ^{208}Pb shells ($Z = 50$, $N = 82$ and $Z = 82$, $N = 126$). For most collision geometries, the initial mass asymmetry increases, which causes the reaction to be characterized as inverse quasifission. In Sec. IV, we provide the analysis of the multinucleon

*ayik@tntech.edu

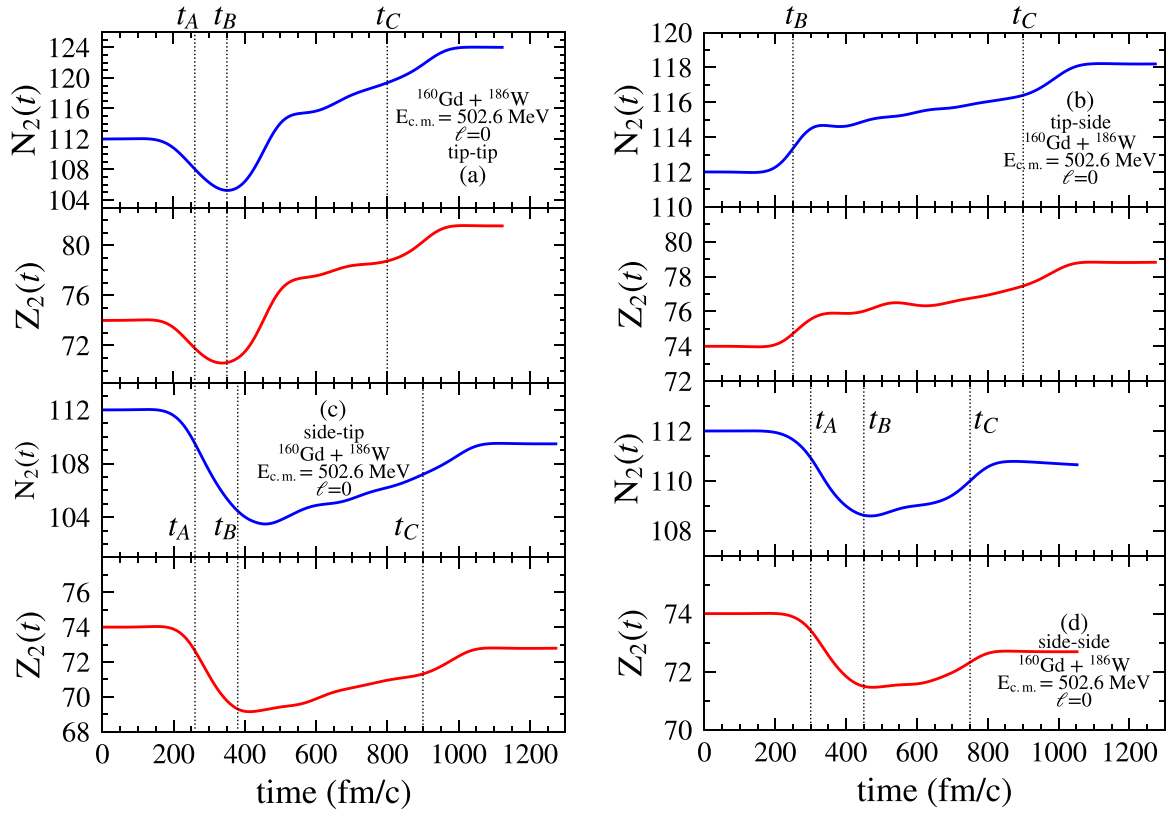

FIG. 1. Mean values of neutron and proton numbers of W-like fragments in the head-on collision of the $^{160}\mathrm{Gd} + {}^{186}\mathrm{W}$ system at $E_{\mathrm{c.m.}} =$ 502.6 MeV in tip-tip (a), tip-side (b), side-tip (c), and side-side (d) geometries.

transfer mechanism for the same reaction. The quantal transport approach describes the production of primary isotopes and we compare results with the available data [53]. The cross-section distributions, mean values, and dispersions are determined without any adjustable parameter employing a Skyrme energy density functional. In Sec. V, we summarize our results and provide conclusions.

II. MEAN-FIELD PROPERTIES

The TDHF theory has been the primary microscopic tool for studying low-energy heavy-ion reactions, including fusion, deep-inelastic collisions, and quasifission [32–36,39–41]. Since the theory is derived by the minimization of the time-dependent many-body action it is deterministic in nature and provides the most probably reaction path for the system. Namely, given a set of initial conditions for the reaction there is only one outcome for the reaction. At some level distribution can be obtained by varying the initial conditions (e.g., orbital angular momentum or the orientation angle for deformed nuclei). However, these distributions are typically much narrower when compared with the experiment [32]. TDHF theory also provides a good description of one-body dissipation [54,55]. In the $^{160}\mathrm{Gd} + {}^{186}\mathrm{W}$ system, initial ground states for the target and the projectile have large prolate deformations. Consequently, the reaction dynamics and the transfer of nucleons depend on the relative alignment of the target and the projectile. We refer to this as the dependence on collision geometry. For the reaction $^{160}\mathrm{Gd} + {}^{186}\mathrm{W}$, at initial energies $E_{\mathrm{c.m.}} = 461.9$ MeV and $E_{\mathrm{c.m.}} = 502.6$ MeV, we explore four distinct alignments of the target and the projectile. Using the convention adopted in the work of Kedziora and Simenel [56], we denote the initial orientation of either the projectile or the target principle deformation axis to be in the beam direction as X, and we denote the case when their principle axis is perpendicular to the beam direction as Y. As a result we are faced with four distinct orientation possibilities for the target and the projectile, labeled as YY, XX, XY, and YX, corresponding to side-side, tip-tip, tip-side, and side-tip collision geometries, respectively (please see Figs. 2 and 3 in Ref. [56]). Here, the first letter stands for the orientation of the lighter collision partner. In Ref. [56], these collision geometries are defined for head-on collisions. In the present work these geometries are adopted for off-central collisions according to the reaction plane. The symmetry axis of the deformed target is placed parallel and perpendicular to the beam direction. Similarly, the symmetry axis of the projectile is placed parallel and perpendicular to the beam direction. In this manner four different collision geometries are labeled in terms of the same notation as for the head-on collisions. Collisions in the YZ geometry are not included in the yield calculations of this work. In a follow-up study we plan to include collisions with this geometry and also the nonlinear effect of the potential energy in yield calculations. The

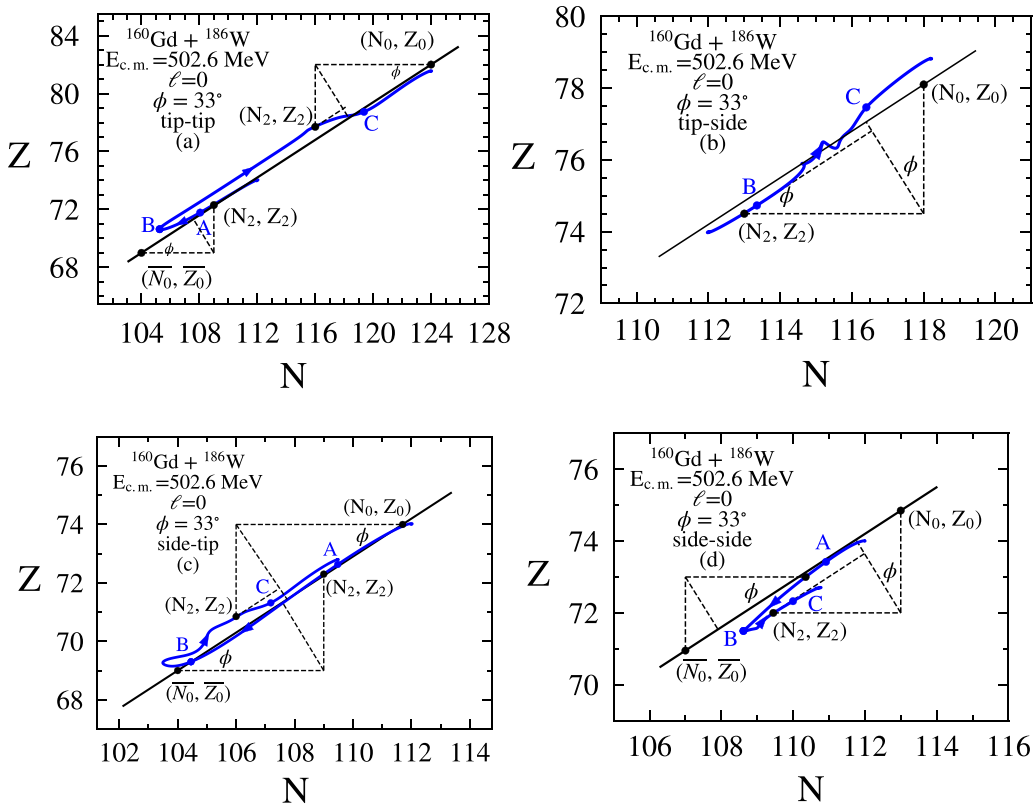

FIG. 2. Blue curves show the drift path of W-like fragments in the head-on collision of the $^{160}\mathrm{Gd} + {}^{186}\mathrm{W}$ system at $E_{\mathrm{c.m.}} = 502.6$ MeV in tip-tip (a), tip-side (b), side-tip (c), and side-side (d) geometries.

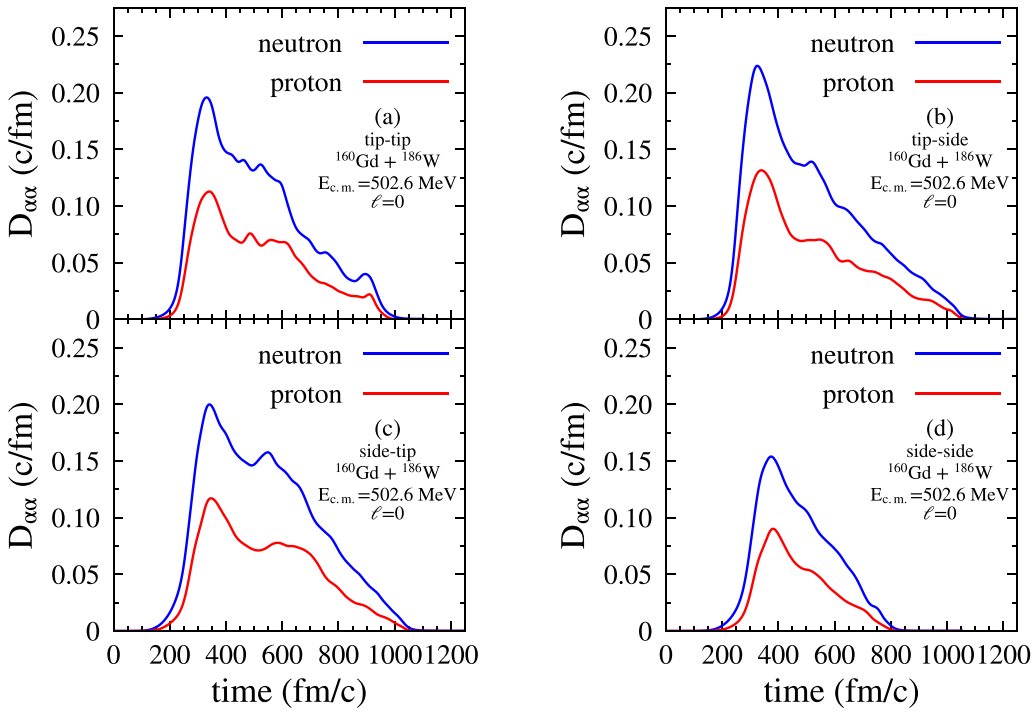

FIG. 3. Neutron and proton diffusion coefficients in the head-on collision of the $^{160}\mathrm{Gd} + {}^{186}\mathrm{W}$ system at $E_{\mathrm{c.m.}} = 502.6$ MeV in tip-tip (a), tip-side (b), side-tip (c), and side-side (d) collision geometries.

TABLE I. Results of the TDHF and SMF calculations for the ^{160}Gd + ^{186}W system at $E_{\text{c.m.}} = 502.6$ MeV in tip-tip (XX), tip-side (XY), side-tip (YX), and side-side (YY) geometries.

Geometry	ℓ_i ($\hbar$)	Z_1^f	A_1^f	Z_2^f	A_2^f	ℓ_f ($\hbar$)	TKEL (MeV)	σ_{NN}	σ_{ZZ}	σ_{NZ}	σ_{AA}	$\theta_{\text{c.m.}}$	θ_1^{lab}	θ_2^{lab}
	120	61.1	152.7	76.9	193.3	117.1	245.7	5.8	4.3	3.9	9.1	120.8	55.0	24.1
	140	64.2	160.5	73.8	185.5	125.2	237.0	5.7	4.3	3.9	9.0	114.3	51.1	27.6
	160	65.8	164.5	72.2	181.5	134.0	208.2	5.6	4.2	3.7	8.8	111.8	51.1	30.0
XX	180	65.5	164.0	72.5	182.0	120.8	173.5	5.4	4.1	3.5	8.4	111.7	53.4	31.0
	200	65.6	164.3	72.4	181.7	138.0	140.5	5.1	3.9	3.2	7.9	107.5	53.2	33.9
	220	65.2	163.5	72.8	182.5	165.9	114.7	4.8	3.5	2.7	7.1	102.8	52.2	36.6
	240	64.5	161.8	73.5	184.2	202.3	85.3	4.1	2.9	1.9	5.7	98.7	51.7	39.1
	120	61.2	152.6	76.8	193.4	116.9	212.3	7.1	4.9	5.2	11.3	120.8	57.9	24.9
	140	64.7	161.6	73.3	184.4	132.8	212.6	6.9	4.8	5.0	11.0	113.6	52.3	28.8
	160	65.4	163.3	72.6	182.7	136.9	186.0	6.6	4.5	4.7	10.4	110.6	52.3	31.1
XY	180	65.3	163.3	72.7	182.7	141.2	169.3	6.2	4.3	4.3	9.7	106.8	51.6	33.2
	200	65.3	163.3	72.7	182.7	154.1	155.3	5.9	4.1	4.0	9.1	102.6	50.3	35.5
	220	65.1	163.0	72.9	183.0	170.6	136.3	5.4	3.8	3.5	8.3	99.0	49.5	37.6
	240	64.9	162.3	73.1	183.7	191.2	113.8	4.8	3.4	2.9	7.1	96.1	49.0	39.6
	260	64.4	161.5	73.6	184.5	218.8	81.9	3.9	2.7	1.9	5.4	94.1	49.3	41.4
	120	66.3	166.3	71.7	179.6	98.1	177.3	6.5	4.6	4.6	10.3	123.2	57.5	26.0
	140	66.1	165.5	71.9	180.5	117.4	162.3	6.2	4.3	4.2	9.6	117.2	56.2	29.0
	160	65.8	164.7	72.2	181.3	130.8	146.4	5.8	4.1	3.9	9.0	112.6	55.3	31.4
YX	180	65.9	165.0	72.1	181.0	148.2	134.2	5.5	3.8	3.5	8.4	107.9	53.5	33.9
	200	65.3	163.8	72.7	182.2	168.5	122.0	5.0	3.5	3.0	7.4	103.6	52.2	36.1
	220	64.5	162.1	73.5	183.9	186.0	101.8	4.4	3.0	2.3	6.3	100.4	51.8	37.9
	240	64.1	161.0	73.9	185.0	217.5	73.5	3.7	2.5	1.6	4.9	97.9	51.8	39.7
	120	64.1	159.8	73.9	186.2	106.7	123.1	5.4	3.7	3.5	8.3	125.7	64.7	25.4
	140	64.4	160.8	73.6	185.2	123.4	113.8	5.1	3.5	3.3	7.7	120.1	62.0	28.3
YY	160	64.6	161.5	73.4	184.5	141.2	105.6	4.8	3.3	2.9	7.2	115.0	59.6	30.9
	180	64.6	161.6	73.4	184.4	159.4	95.6	4.5	3.1	2.6	6.5	110.6	57.7	33.2
	200	64.4	161.4	73.6	184.6	175.4	81.4	4.0	2.8	2.1	5.7	106.9	56.3	35.3
	220	64.3	161.2	73.7	184.8	193.2	66.3	3.6	2.4	1.6	4.8	103.7	55.3	37.1

calculations presented in the rest of the article employed the TDHF code [57,58] using the SLy4d Skyrme energy density functional [59], with a box size of $60 \times 60 \times 36$ fm in the x, y, and z directions, respectively. The results of our TDHF calculations for all of these collision geometries are tabulated in Tables I and II at two bombarding energies and for a range of initial orbital angular momenta ℓ_i. We denote the final values of mass and charge numbers for the Gd-like fragments with A_1^f and Z_1^f, W-like fragments with A_2^f and Z_2^f, final total kinetic energy lost (TKEL), scattering angles in the center-of-mass (c.m.) ($\theta_{\text{c.m.}}$) and laboratory frame (θ_1^{lab} and θ_2^{lab}). These tables also include asymptotic values of neutron σ_{NN}, proton σ_{ZZ}, mixed dispersions σ_{NZ}, and mass dispersions σ_{AA}, which are discussed in Sec. III. To economize on the computation time, all quantities are evaluated in steps of 20 units of orbital angular momentum. The range of initial orbital angular momenta is specified according to the angular position of detectors in the laboratory system. The values of initial orbital angular momenta, which fall into the detector acceptance range of 25°–65° in the laboratory frame, are shown in Tables I and II. At the lower collision energy, $E_{\text{c.m.}} = 461.9$ MeV, only in the tip-tip and tip-side geometries do produced fragments fall in the acceptance range of detectors. As a result, in Table II only the tip-tip and tip-side results are shown. Different collision geometries have qualitatively distinct nucleon transfer mechanisms. These can be seen more clearly by plotting the

TABLE II. Results of the TDHF and SMF calculations for the ^{160}Gd + ^{186}W system at $E_{\text{c.m.}} = 461.9$ MeV in tip-tip (XX) and tip-side (XY) geometries.

Geometry	ℓ_i ($\hbar$)	Z_1^f	A_1^f	Z_2^f	A_2^f	ℓ_f ($\hbar$)	TKEL (MeV)	σ_{NN}	σ_{ZZ}	σ_{NZ}	σ_{AA}	$\theta_{\text{c.m.}}$	θ_1^{lab}	θ_2^{lab}
	140	65.0	162.6	73.0	183.4	88.9	97.7	5.1	3.8	3.1	7.7	129.7	65.8	23.8
XX	160	64.9	162.7	73.1	183.3	116.1	81.4	4.7	3.5	2.7	7.0	123.3	63.7	27.1
	180	64.4	161.5	73.6	184.5	149.7	56.7	4.1	3.0	2.0	5.8	117.9	62.6	30.1
	140	64.6	161.8	73.4	184.2	117.2	75.2	4.8	3.3	2.8	7.1	126.3	66.0	25.7
XY	160	64.5	161.7	73.5	184.3	138.2	59.2	4.3	3.0	2.3	6.1	121.3	64.3	28.4

time evolution of neutron $N(t)$ and proton $Z(t)$ numbers for Gd-like fragments or W-like fragments. In Fig. 1, time evolutions of proton and neutron numbers of W-like fragments in the central collision of ^{160}Gd + ^{186}W are presented at different collision geometries.

We can extract more useful information about nucleon transfer mechanisms by examining drift paths. Drift paths are obtained by eliminating time from neutron numbers $N(t)$ and proton numbers $Z(t)$ and plotting the result in the (N, Z) plane. Drift paths in different collision geometries exhibit a different behavior as a result of the shell effects on the dynamics, and they contain specific information about the time evolution of the mean values of macroscopic variables. In Fig. 2 we plot drift paths for head-on collisions in different geometries for W-like fragments (blue curves). In these figures, thick black lines denote sets of fragments with a charge asymmetry value of $\frac{N-Z}{N+Z} = 0.20$. These lines are called the isoscalar path, which travels near the bottom of the stability valley. The isoscalar path extends all the way from the lead valley on the upper end to the barium valley on the lower end, and it makes about $\phi = 33^\circ$ with the horizontal neutron axis. We observe that, in all geometries, W-like fragments drift along the isoscalar direction with a charge asymmetry of approximately 0.20. Figure 2(a) shows the drift path in tip-tip (XX) collisions. Initially, as seen usually in quasifission reactions, W-like heavy fragments lose nucleons and the system drifts toward symmetry. After this initial behavior, W-like heavy fragments turn back and by gaining nucleons drift toward asymmetry. This kind of drift path is not very usual and it is referred to as an inverse quasifission reaction. Figure 2(b) shows the drift path in the tip-side (XY) collision. In this case, the drift path also indicates an inverse quasifission reaction. In the side-tip (YX) collision, shown in Fig. 2(c), the nucleon drift mechanism is similar to the tip-tip (XX) geometry. Initially, heavy fragments lose neutrons and protons and the system drifts along the isoscalar path toward symmetry, subsequently changing direction and drifting toward asymmetry. As seen in Fig. 2(d), in the side-side (YY) collision, the drift mechanism is analogous to the one for the side-tip collision.

III. QUANTAL DIFFUSION OF NUCLEON TRANSFER

A. Langevin equations for multinucleon transfer

In TDHF theory, with a prescribed set of initial conditions, the many-body state is a single Slater determinant and a unique single-particle density matrix, which is time-dependent, describing the deterministic reaction path for the dynamical system. In beyond-TDHF approaches, the introduction of additional correlations is typically represented by a superposition of Slater determinants. In the SMF theory, correlations are introduced as fluctuations of the initial state, which constitute an ensemble of single-particle density matrices [47,48]. For each of these single-particle density matrices in the ensemble, the time evolution reduces to the TDHF equations initialized by the self-consistent Hamiltonian of the particular event. In constructing the fluctuations of these initial density matrices, SMF employs a Gaussian distribution of the random elements with variances that are specified with the requirement that the ensemble averages of the one-body operator dispersions of the initial state are the same as the ones obtained in the quantal expressions in the mean-field approach.

For low-energy heavy-ion collisions at energies near the Coulomb barrier the dynamical system generally maintains a dinuclear configuration. In these cases instead of generating an ensemble of mean-field events one can formulate a more straightforward transport approach. Using the window dynamics of the dinuclear system one can do a geometric projection of the SMF approach to obtain Langevin equations for the relevant macroscopic variables. Fragments at each time step are defined in terms of the window dynamics. The symmetry axis of the dinuclear complex is determined by calculating the mass quadrupole moment of the system at different time steps. The principle axis of the quadrupole tensor indicates the symmetry axis of the dinuclear complex. The window plane is perpendicular to the symmetry axis and passes through the lowest density point in the neck area. Density integrals of the right and left sides of the window plane define the projectilelike and targetlike fragments. The window plane and its orientation continuously change during the rotation of the dinuclear complex. For the derivations of the quantal diffusion formalism and the utilization of window dynamics we refer the reader to earlier references [60–66]. Neutron and proton numbers of the projectilelike or targetlike fragment are chosen as the relevant macroscopic variables to formulate the diffusion formalism. For the system at hand, we take neutron $N_2^\lambda(t)$ and proton $Z_2^\lambda(t)$ numbers of the W-like fragments as relevant macroscopic variables. For each event λ, the fragment neutron and proton numbers are obtained by integrating the density on the left and the right of the window. During the contact phase, fragment proton and neutron numbers fluctuate between events as a result of random nucleon flux through the window. These numbers can be decomposed as fluctuations about the mean values as $N_2^\lambda(t) = N_2(t) + \delta N_2^\lambda(t)$ and $Z_2^\lambda(t) = Z_2(t) + \delta Z_2^\lambda(t)$. Here, $N_2(t)$ and $Z_2(t)$ are the mean values obtained over the ensemble of SMF events.

These mean values can be deduced from the mean-field TDHF calculations for small-amplitude fluctuations. In the quantal diffusion approach, for small-amplitude fluctuations, neutron $\delta N_2^\lambda(t)$ numbers and proton $\delta Z_2^\lambda(t)$ numbers evolve according to a coupled linear set of quantal Langevin equations,

$$\frac{d}{dt}\begin{pmatrix}\delta Z_2^\lambda(t)\\ \delta N_2^\lambda(t)\end{pmatrix} = \begin{pmatrix}\frac{\partial v_p}{\partial Z_2}\left(Z_2^\lambda - Z_2\right) + \frac{\partial v_p}{\partial N_2}\left(N_2^\lambda - N_2\right)\\ \frac{\partial v_n}{\partial Z_2}\left(Z_2^\lambda - Z_2\right) + \frac{\partial v_n}{\partial N_2}\left(N_2^\lambda - N_2\right)\end{pmatrix} + \begin{pmatrix}\delta v_p^\lambda(t)\\ \delta v_n^\lambda(t)\end{pmatrix}. \quad (1)$$

The quantities $v_\alpha^\lambda(t) = v_\alpha(t) + \delta v_\alpha^\lambda(t)$ denote the drift coefficients for protons and neutrons, with the mean values and the fluctuating parts given by $v_\alpha(t)$ and $\delta v_\alpha^\lambda(t)$, respectively. Here, the index α labels protons and neutrons. Drift coefficients $v_\alpha^\lambda(t)$ denote the rate of flux for protons and neutrons through the window in event λ. The linear limit of the Langevin description employed here proved to be a good approximation when the driving potential energy was more or less harmonic

around equilibrium values of the mass and charge asymmetries. In the first term of the Langevin equations, Eq. (1), deviations of drift coefficients from the local equilibrium state should appear. These deviations are related to the potential energy surface of the dinuclear complex in the (N-Z) plane. In this paper, and previous studies, we have approximated the potential energy in the vicinity of the local equilibrium to be a parabolic form. This leads to the linear form of the Langevin equations as seen in Eq. (1). The most useful fact of using Einstein relations is that it is possible to extract curvature parameters in terms of drift and diffusion information, which are determined from microscopic TDHF solutions, without using adjustable parameters. So far, this linear approximation has appeared to provide a good approximation in comparison with data. However, it is possible to improve the harmonic form of the potential energy by adding access and skewness terms, which provide a better description of large-amplitude fluctuations. This is one of the projects we are working on to improve the quantal transport description for the nucleon transfer mechanism. The rate of change of neutron and proton numbers determines the mean values of drift coefficients. For W-like fragments, these are shown in Fig. 1. Quantal expressions for the stochastic parts of the drift coefficients $\delta v_\alpha^\lambda(t)$ can be found in Refs. [67,68].

B. Quantal diffusion coefficients

Stochastic parts of the drift coefficients $\delta v_p^\lambda(t)$ and $\delta v_n^\lambda(t)$ are the primary generator of fluctuations in charge and mass asymmetry degrees of freedom. In the SMF theory, these stochastic parts of drift coefficients are Gaussian random distributions centered about a zero mean value, $\delta\overline{v}_{p,n}^\lambda(t) = 0$. The autocorrelation functions of the stochastic drift coefficient, written as an integration over the evolution history, give the diffusion coefficients $D_{\alpha\alpha}(t)$ for proton and neutron transfer:

$$\int_0^t dt' \overline{\delta v_\alpha^\lambda(t')\delta v_\alpha^\lambda(t)} = D_{\alpha\alpha}(t). \tag{2}$$

In the most general formulation, the diffusion coefficients are over a complete set of particle-hole states. In the diabatic limit we can get rid of the particle states by utilizing closure relations. As a consequence, the diffusion coefficients are then obtained solely in terms of the occupied single-particle states of the TDHF calculations, which provides a significant simplification. Our previous publications provide all the explicit expressions for the diffusion coefficients [60–68]. The analysis of these coefficients are also provided in Appendix B of Ref. [61]. The determination of the diffusion coefficients by virtue of the mean-field properties is consistent with the fluctuation-dissipation theorem of nonequilibrium statistical mechanics and it significantly uncomplicates the calculation of quantal diffusion coefficients. Quantal properties, such as shell effects, the Pauli principle, and the effect of the unrestricted collision geometry, are included in these diffusion coefficients without any adjustable parameters. We point out that there is a close analogy between the quantal expression and the classical diffusion coefficient for a random walk problem [69–71]. The direct part is given as the sum of the nucleon currents across the window from the projectilelike fragment to the targetlike fragment and from the targetlike fragment to the projectilelike fragment, integrated over the memory. This is analogous to the random walk problem, in which the diffusion coefficient is given by the sum of the rate of the forward and backward steps. The Pauli blocking effect in the transfer mechanism does not have a classical counterpart and is represented in the second part of the quantal diffusion equations. This is illustrated in Fig. 3, where we plot the neutron and proton diffusion coefficients in head-on collisions of the ^{160}Gd + ^{186}W system at $E_{\text{c.m.}} = 502.6$ MeV for different collision geometries.

C. Potential energy of the dinuclear system

The nucleon drift mechanism and dispersions of fragment distributions are determined in terms of two competing effects: (i) nucleon diffusion tends to increase the dispersion of distribution functions, and (ii) the potential energy of the dinuclear system $U(N_2, Z_2)$ on the neutron and proton plane that controls the mean nucleon drift and determines the saturation values of dispersions. The potential energy of the dinuclear system consists mainly of electrostatic energy, symmetry energy, surface energy, and centrifugal energy. The TDHF theory encompasses different energy contributions at the microscopic level. Furthermore, TDHF calculations illustrate that the potential energy depends on the geometry of the dinuclear system. It is possible to extract useful information about the potential energy with the help of the Einstein relation in the overdamped limit [60–64]. In the overdamped limit, drift coefficients are related to the potential energy surface in the (N, Z) plane as

$$v_n(t) = -\frac{D_{NN}(t)}{T^*}\frac{\partial}{\partial N_2}U(N_2, Z_2), \tag{3a}$$

$$v_z(t) = -\frac{D_{ZZ}(t)}{T^*}\frac{\partial}{\partial Z_2}U(N_2, Z_2), \tag{3b}$$

where T^* stands for the effective temperature of the system, and N_2 and Z_2 indicate the neutron and proton numbers of W-like fragments in the dinuclear system. The drift information of the ^{160}Gd + ^{186}W system gives information about the potential energy only in the isoscalar direction. To obtain information about the potential energy in the direction perpendicular to the stability valley, we consider the collision of a neighboring ^{172}Gd + ^{174}W system at $E_{\text{c.m.}} = 502.6$ MeV.

Figure 4 shows the drift paths of W-like fragments in head-on collisions in different geometries. In all geometries, the system rapidly follows a path nearly perpendicular to the stability valley to reach charge asymmetry equilibrium. We refer to the direction perpendicular to the stability valley as the isovector direction. Evolution in the isovector direction is accompanied by drift along the isoscalar path toward symmetry or asymmetry. At the end of the relatively short contact time, the system separates before reaching the local equilibrium state.

In collisions of the ^{160}Gd + ^{186}W system, a heavier local equilibrium state is in the vicinity of the lead valley with neutron and proton numbers around $N_0 = 124$ and $Z_0 = 82$, while the lighter local equilibrium state is in the neighborhood of the barium valley, having neutron and proton numbers

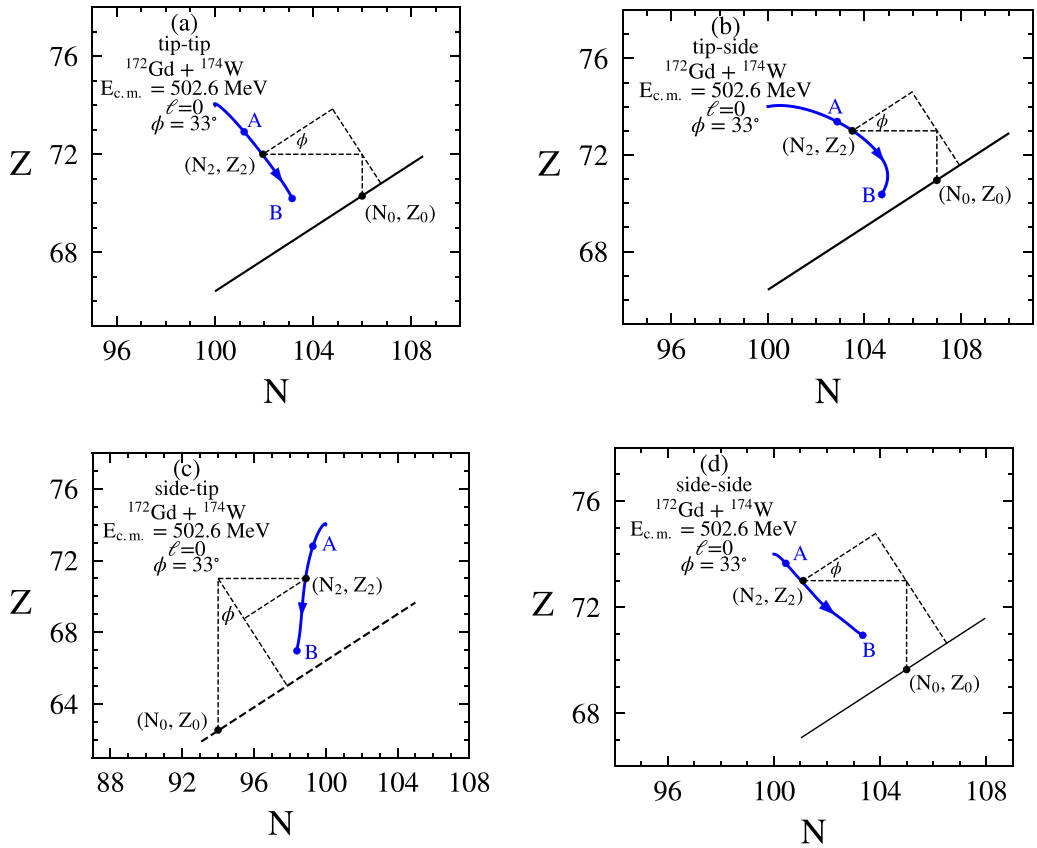

FIG. 4. Blue curves show the drift paths of W-like fragments in the head-on collision of the ^{172}Gd + ^{174}W system at $E_{\text{c.m.}} = 502.6$ MeV in tip-tip (a), tip-side (b), side-tip (c), and side-side (d) geometries.

near $\overline{N_0} = 84$ and $\overline{Z_0} = 56$. These nuclei are located on the isoscalar path with a charge asymmetry of 0.20. The drift information of these two similar systems, when combined, can provide an approximate description of the potential energy surface of the dinuclear system relative to the equilibrium value of the potential energy in terms of two parabolic forms,

$$U(N_2, Z_2) = \tfrac{1}{2} a R_S^2(N_2, Z_2) + \tfrac{1}{2} b R_V^2(N_2, Z_2). \tag{4}$$

Here, $R_S(N_2, Z_2)$ and $R_V(N_2, Z_2)$ represent perpendicular distances of a fragment with neutron and proton numbers (N_2, Z_2) from the isoscalar path and from the local equilibrium state along the isoscalar path, respectively. For ^{160}Gd + ^{186}W collisions, in particular, tip-tip and tip-side collisions W-like fragments appear to drift towards the ^{206}Pb local equilibrium state due to the $Z = 82$ shell effect in the lead valley. There are also octupole shell effects in the $Z = 56$ barium isotopes as discussed in Ref. [72]. Most probably both shell effects act as a driving force toward asymmetry.

As a consequence of the sharp increase in the asymmetry energy, we anticipate the isovector curvature parameter to be considerably greater than the corresponding isoscalar curvature parameter. From the geometry of Figs. 2 and 4, we express isovector and isoscalar distances in terms of neutron and proton numbers of the fragment and neutron and proton numbers of the equilibrium states. When drift is in the asymmetry direction, the isoscalar distance is given by $R_V(t) = [N_0 - N_2(t)]\cos\phi + [Z_0 - Z_2(t)]\sin\phi$, and for drift in the symmetry direction, it is given by $\overline{R_V}(t) = [N_2(t) - \overline{N_0}]\cos\phi + [Z_2(t) - \overline{Z_0}]\sin\phi$. In both cases, the isovector distance is given by $R_S(t) = [N_0 - N_2(t)]\sin\phi - [Z_0 - Z_2(t)]\cos\phi$. The angle ϕ is the angle between the isoscalar path and the N axis, which is about $\phi = 33^\circ$.

Mean drift coefficients and diffusion coefficients are determined from the TDHF and SMF calculations; using Einstein relations in Eq. (3), we can determine the reduced curvature coefficients $\alpha = a/T^*$ and $\beta = b/T^*$. Only ratios of the curvature parameters and the effective temperature appear. As a result, the effective temperature is not a parameter in the description. The reduced curvature parameters in each collision geometry vary in time due to the shell structure of the TDHF description. In calculations of dispersion values we employ constant curvature parameters, which are determined by averaging over suitable time intervals when the overlap between the colliding nuclei is sufficiently large. When drift occurs toward asymmetry, the averaged value of the isoscalar reduced curvature parameter over time intervals t_B and t_C is determined as

$$\beta^{\text{asym}} = \frac{1}{R_V^{\text{asym}}} \int_{t_B}^{t_C} \left(\frac{v_n(t)\cos\phi}{D_{NN}(t)} + \frac{v_p(t)\sin\phi}{D_{ZZ}(t)} \right) dt, \tag{5}$$

TABLE III. Calculation of the β curvature parameter using the ^{160}Gd + ^{186}W system at $E_{\text{c.m.}} = 502.6$ MeV in tip-tip (XX), tip-side (XY), side-tip (YX), and side-side (YY) geometries. The time intervals t_A, t_B, and t_C required to calculate isoscalar curvature parameters are shown in Fig. 1. All times are in units of fm/c. Calculation of the α curvature parameter are shown in Fig. 5.

^{160}Gd + ^{186}W	t_A	t_B	t_C	β_{AB}^{sym}	β_{BC}^{asym}	$\overline{\beta} = (\beta_{AB}^{\text{sym}} + \beta_{BC}^{\text{asym}})/2$
Tip-tip	260	350	800	0.010	0.034	0.022
Tip-side	—	250	900	—	0.008	0.008
Side-tip	260	380	900	0.016	0.004	0.010
Side-side	300	450	750	0.007	0.010	0.009

where the integrated value of the isoscalar distance for the drift towards asymmetry is given by

$$R_V^{\text{asym}} = \int_{t_B}^{t_C} \{[\,N_0 - N_2(t)\,]\cos\phi + [\,Z_0 - Z_2(t)\,]\sin\phi\}dt. \tag{6}$$

When the drift occurs toward symmetry, we can determine the averaged value of the isoscalar reduced curvature parameter over time intervals t_A and t_B as

$$\beta^{\text{sym}} = -\frac{1}{R_V^{\text{sym}}}\int_{t_A}^{t_B}\left(\frac{v_n(t)\cos\phi}{D_{NN}(t)} + \frac{v_p(t)\sin\phi}{D_{ZZ}(t)}\right)dt, \tag{7}$$

where the integrated value of the isoscalar distance for the drift towards symmetry is given by

$$R_V^{\text{sym}} = \int_{t_A}^{t_B} \{[\,N_2(t) - \overline{N_0}\,]\cos\phi + [\,Z_2(t) - \overline{Z_0}\,]\sin\phi\}dt. \tag{8}$$

These expressions can be used to calculate the averaged values of the isoscalar reduced curvature parameters in different geometries. In Table III, the calculated values of isoscalar reduced curvature parameters for different geometries are given. In tip-tip, side-tip, and side-side geometries, initially a drift towards symmetry is observed, followed by a drift towards asymmetry. For these geometries, we determine the isoscalar curvature parameter by taking the average of the drift towards symmetry part and the drift towards asymmetry part, given as $\overline{\beta} = (\beta_{AB}^{\text{sym}} + \beta_{BC}^{\text{asym}})/2$.

We estimate the isovector reduced curvature parameters in different geometries from the drift paths of the ^{172}Gd + ^{174}W system at $E_{\text{c.m.}} = 502.6$ MeV by averaging over time intervals t_A and t_B as

$$\alpha = \frac{1}{R_S}\int_{t_A}^{t_B}\left(\frac{v_n(t)\sin\phi}{D_{NN}(t)} - \frac{v_p(t)\cos\phi}{D_{ZZ}(t)}\right)dt, \tag{9}$$

where the integrated value of the isovector distance is given by

$$R_S = \int_{t_A}^{t_B} \{[\,N_0 - N_2(t)\,]\sin\phi - [\,Z_0 - Z_2(t)\,]\cos\phi\}dt. \tag{10}$$

Using Eq. (9), diffusion coefficients for the ^{172}Gd + ^{174}W system at $E_{\text{c.m.}} = 502.6$ MeV are plotted in Fig. 6.

We can use these expressions in calculating averaged values of isovector reduced curvature parameters in different geometries. In Table IV, the calculated values of isovector reduced curvature parameters for different geometries are given. The potential energy surface in the (N-Z) plane should not depend on the centrifugal potential energy and the excitation energy of the dinuclear system. Therefore, in the ^{160}Gd + ^{186}W system at $E_{\text{c.m.}} = 461.9$ MeV, we employ the same curvature parameters that are determined at $E_{\text{c.m.}} = 502.6$ MeV. Since the drift coefficients have an analytical form, we can immediately determine their derivatives to find the following:

$$\frac{\partial v_n}{\partial N_2} = -D_{NN}(\alpha\sin^2\phi + \beta\cos^2\phi), \tag{11}$$

$$\frac{\partial v_z}{\partial Z_2} = -D_{ZZ}\big(\alpha\cos^2\phi + \beta\sin^2\phi\big), \tag{12}$$

$$\frac{\partial v_n}{\partial Z_2} = -D_{NN}(\beta - \alpha)\sin\phi\cos\phi, \tag{13}$$

$$\frac{\partial v_z}{\partial N_2} = -D_{ZZ}(\beta - \alpha)\sin\phi\cos\phi. \tag{14}$$

The curvature parameter α perpendicular to the β-stability valley is much larger than the curvature parameter β along the stability valley. Consequently, β does not have an appreciable effect on the derivatives of the drift coefficients. These derivative expressions are needed to calculate neutron, proton, and mixed dispersions, as discussed in the following section.

D. Fragment probability distributions

In general, the combined probability distribution function $P_\ell(N, Z)$ for producing a fragment with neutron N and proton Z is obtained by producing a large number of solutions of the Langevin equation (1). The equivalence between the Langevin equation and the Fokker-Planck equation for the distribution function of the macroscopic variables [70] is of common knowledge. When the drift coefficients are linear

TABLE IV. Calculation of the α curvature parameter using the ^{172}Gd + ^{174}W system at $E_{\text{c.m.}} = 502.6$ MeV in tip-tip (XX), tip-side (XY), side-tip (YX), and side-side (YY) geometries. The time intervals t_A and t_B required to calculate isovector curvature parameters are shown in Fig. 5. All times are in units of fm/c.

^{172}Gd + ^{174}W	t_A	t_B	α
Tip-tip	180	260	0.113
Tip-side	250	400	0.133
Side-tip	200	350	0.127
Side-side	250	450	0.143

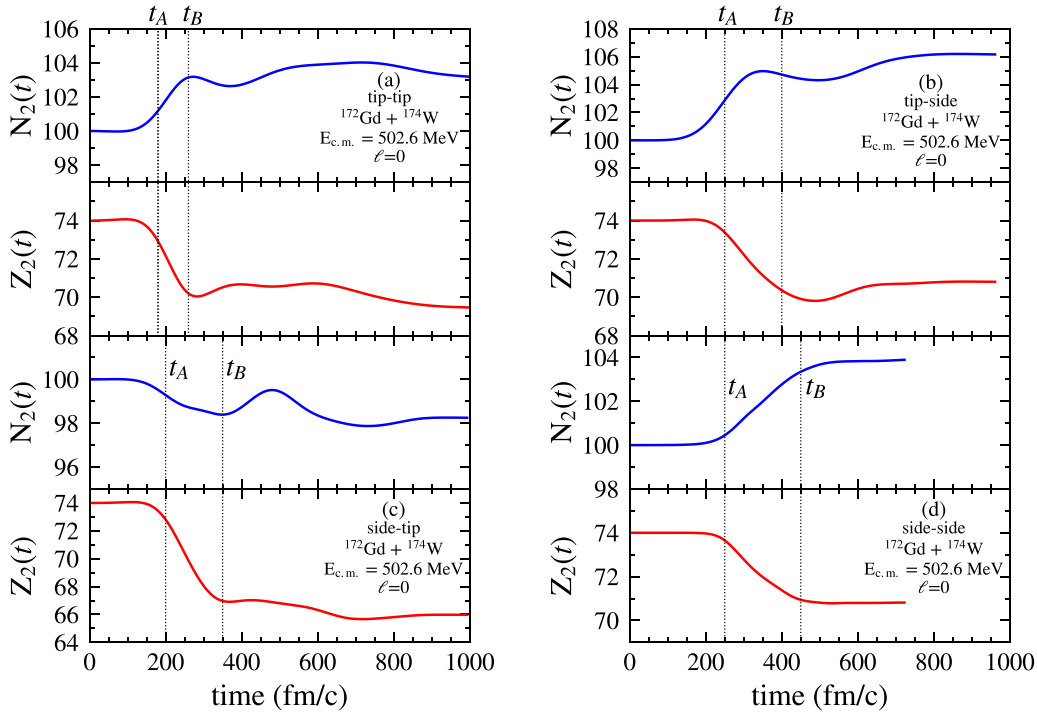

FIG. 5. Mean values of neutron and proton numbers of W-like fragments in the head-on collision of the $^{172}\mathrm{Gd} + {}^{174}\mathrm{W}$ system at $E_{\mathrm{c.m.}} = 502.6$ MeV in tip-tip (a), tip-side (b), side-tip (c), and side-side (d) geometries.

functions of macroscopic variables, as in the case of Eq. (1), the proton and neutron distribution functions for the initial angular momentum ℓ are given as a correlated Gaussian function described by the mean values, and the neutron, proton, and mixed dispersions, as

$$P_\ell(N,Z) = \frac{1}{2\pi\sigma_{NN}(\ell)\sigma_{ZZ}(\ell)\sqrt{1-\rho_\ell^2}} \exp\left(-C_\ell\right). \quad (15)$$

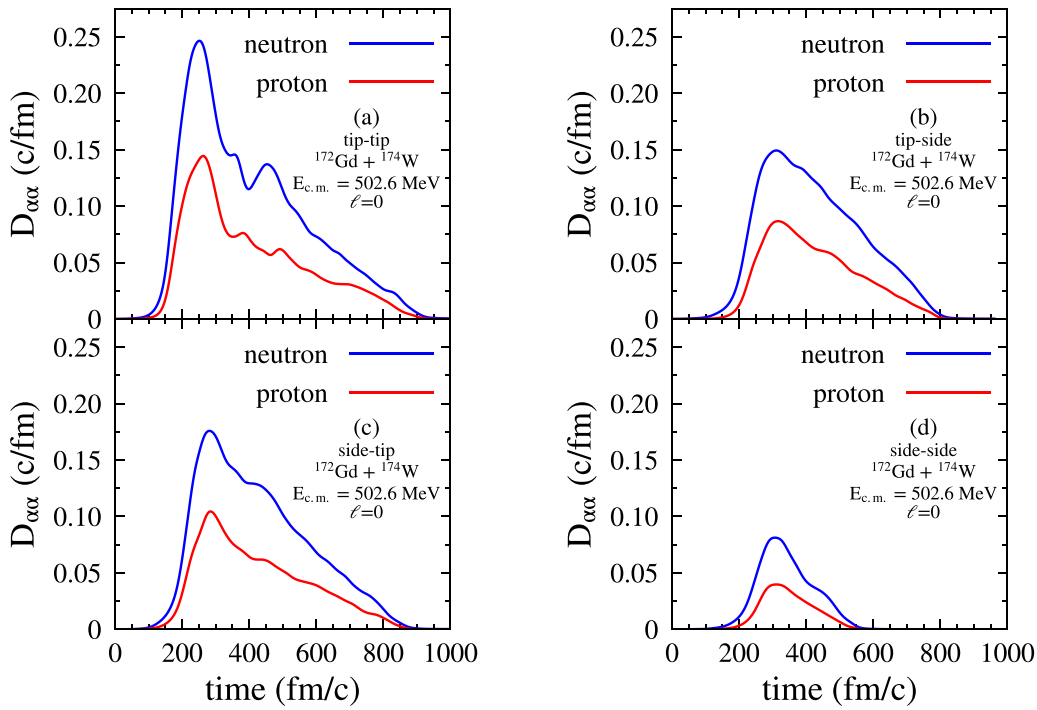

FIG. 6. Diffusion coefficients in the head-on collision of the $^{172}\mathrm{Gd} + {}^{174}\mathrm{W}$ system at $E_{\mathrm{c.m.}} = 502.6$ MeV in tip-tip (a), tip-side (b), side-tip (c), and side-side (d) geometries.

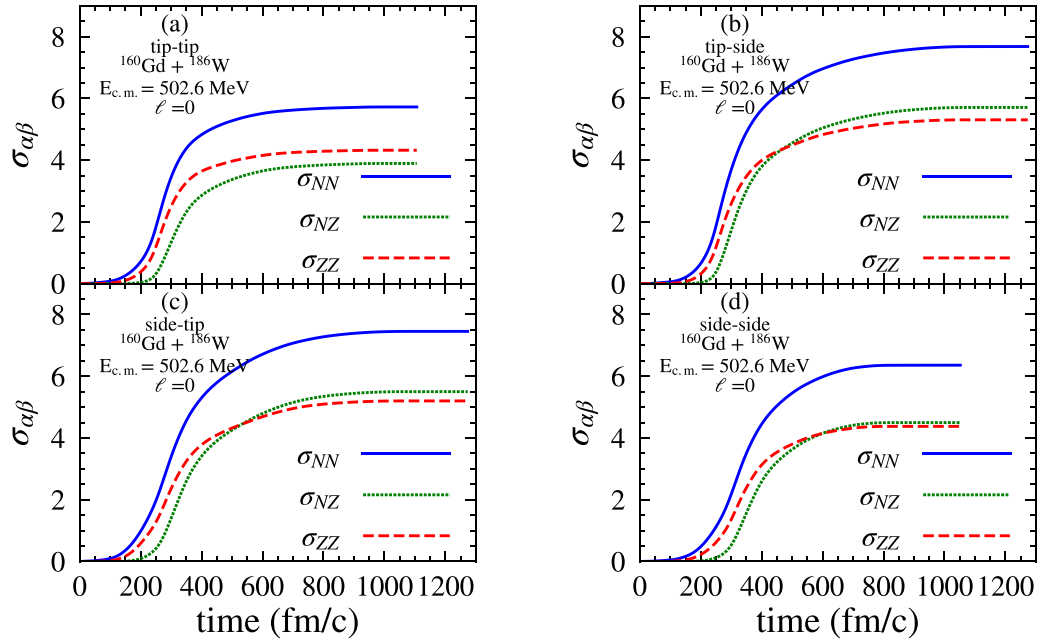

FIG. 7. Neutron, proton, and mixed variances as a function of time in the head-on collision of the ^{160}Gd + ^{186}W system at $E_{\text{c.m.}} = 502.6$ MeV in tip-tip (a), tip-side (b), side-tip (c), and side-side (d) geometries.

Here, the exponent C_ℓ is given by

$$C_\ell = \frac{1}{2\left(1-\rho_\ell^2\right)}\left[\left(\frac{Z-Z_\ell}{\sigma_{ZZ}(\ell)}\right)^2 - 2\rho_\ell\left(\frac{Z-Z_\ell}{\sigma_{ZZ}(\ell)}\right)\left(\frac{N-N_\ell}{\sigma_{NN}(\ell)}\right) + \left(\frac{N-N_\ell}{\sigma_{NN}(\ell)}\right)^2\right], \tag{16}$$

with the correlation coefficient defined as $\rho_\ell = \sigma^2_{\text{NZ}}(\ell)/[\sigma_{\text{ZZ}}(\ell)\sigma_{\text{NN}}(\ell)]$. The quantities $N_\ell = \overline{N}^\lambda_\ell$ and $Z_\ell = \overline{Z}^\lambda_\ell$ denote the mean neutron and proton numbers of the targetlike or projectlike fragments. These mean values are obtained by performing TDHF calculations. It is possible to deduce coupled differential equations for variances $\sigma^2_{\text{NN}}(\ell) = \overline{\delta N^\lambda \delta N^\lambda}$ and $\sigma^2_{\text{ZZ}}(\ell) = \overline{\delta Z^\lambda \delta Z^\lambda}$ and covariances $\sigma^2_{\text{NZ}}(\ell) = \overline{\delta N^\lambda \delta Z^\lambda}$ by multiplying the Langevin equation (1) with δN^λ and δZ^λ and carrying out the average over the ensemble generated from the solution of the Langevin equation. These coupled equations were obtained in Refs. [60–65,73]. We provide these differential equations here again for completeness [74],

$$\frac{\partial}{\partial t}\sigma^2_{NN} = 2\frac{\partial \nu_n}{\partial N_2}\sigma^2_{NN} + 2\frac{\partial \nu_n}{\partial Z_2}\sigma^2_{NZ} + 2D_{NN}, \tag{17}$$

$$\frac{\partial}{\partial t}\sigma^2_{ZZ} = 2\frac{\partial \nu_p}{\partial Z_2}\sigma^2_{ZZ} + 2\frac{\partial \nu_p}{\partial N_2}\sigma^2_{NZ} + 2D_{ZZ}, \tag{18}$$

and

$$\frac{\partial}{\partial t}\sigma^2_{NZ} = \frac{\partial \nu_p}{\partial N_2}\sigma^2_{NN} + \frac{\partial \nu_n}{\partial Z_2}\sigma^2_{ZZ} + \sigma^2_{NZ}\left(\frac{\partial \nu_p}{\partial Z_2} + \frac{\partial \nu_n}{\partial N_2}\right). \tag{19}$$

The set of coupled equations are also familiar from the phenomenological nucleon exchange model, and they were derived from the Fokker-Planck equation for the fragment neutron and proton distributions in the deep-inelastic heavy-ion collisions [71,74]. Variances and covariances are determined from the solutions of these coupled differential equations with the initial conditions $\sigma^2_{NN}(t=0) = 0$, $\sigma^2_{ZZ}(t=0) = 0$, and $\sigma^2_{NZ}(t=0) = 0$ for each angular momentum ℓ. As an example, Fig. 7 shows neutron, proton, and mixed dispersions in ^{160}Gd + ^{186}W collisions with the initial angular momentum $\ell = 0\hbar$ at $E_{\text{c.m.}} = 502.6$ MeV for different geometries. The probability distribution of the mass number of produced fragments is determined by summing over N or Z and keeping the total mass number constant $A = N + Z$:

$$P_\ell(A) = \frac{1}{\sqrt{2\pi}\sigma_{AA}}\exp\left[\frac{-1}{2}\left(\frac{A-A_\ell}{\sigma_{AA}(\ell)}\right)^2\right], \tag{20}$$

where the mass variance is given by $\sigma^2_{AA} = \sigma^2_{NN} + \sigma^2_{ZZ} + 2\sigma^2_{NZ}$.

IV. PRODUCTION CROSS SECTIONS OF PRIMARY FRAGMENTS

It is possible to calculate double cross sections as a function of neutron and proton numbers of primary fragments. In the experimental analysis of Kozulin *et al.* [53], only the mass distribution of primary fragments is published. Therefore, we present the calculation of cross sections $\sigma^s(A)$ as a function of the mass number A of primary fragments using the familiar expression

$$\sigma^s(A) = \frac{\pi\hbar^2}{2\mu E_{\text{c.m.}}}\sum_{\ell_{\min}}^{\ell_{\max}}(2\ell+1)P^s_\ell(A), \tag{21}$$

with

$$P^s_\ell(A) = \tfrac{1}{2}\left[P^s_{\ell,\text{pro}}(A) + P^s_{\ell,\text{tar}}(A)\right]. \tag{22}$$

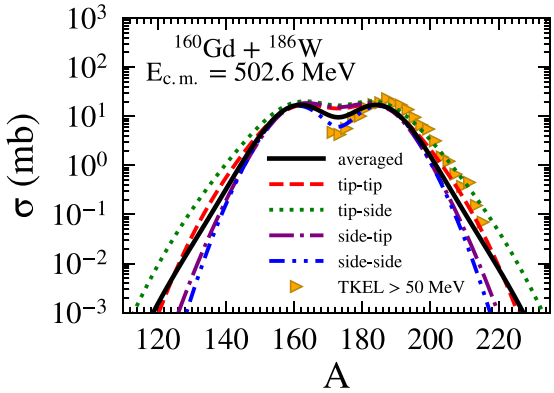

FIG. 8. Total cross sections in collisions of the $^{160}\mathrm{Gd} + {}^{186}\mathrm{W}$ system at $E_{\mathrm{c.m.}} = 502.6$ MeV as a function of the mass number A. Different geometries are indicated by dashed (red), dotted (green), dashed-dotted (purple), and dashed-dot-dotted (blue) lines. Average cross-section and experimental data taken from Ref. [53] are indicated by the solid black line and yellow triangles, respectively.

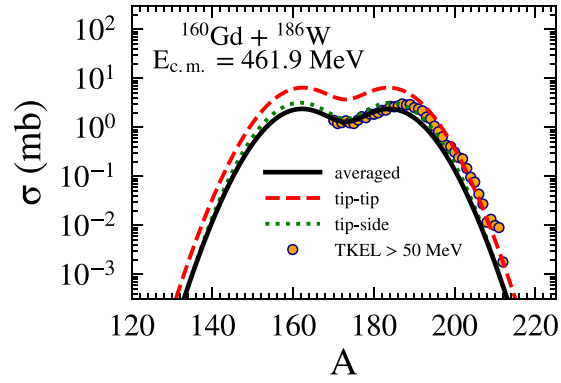

FIG. 9. Total cross section in collisions of the $^{160}\mathrm{Gd} + {}^{186}\mathrm{W}$ system at $E_{\mathrm{c.m.}} = 461.9$ MeV as a function of the mass number A. Different geometries are indicated by dotted (green) and dashed (red) lines. Average cross-section and experimental data taken from Ref. [53] are indicated by the solid black line and yellow circles, respectively.

Here the label "s" indicates the different geometries of the collisions. In this expression, $P^{s}_{\ell,\mathrm{pro}}(A)$ and $P^{s}_{\ell,\mathrm{tar}}(A)$ denote the normalized probability of producing projectilelike and targetlike fragments. These probabilities are given by Eq. (20) with mean values of projectilelike and targetlike fragments, respectively. To make the total primary fragment distribution normalized to unity we multiply by a factor of $1/2$. In summation over the initial angular momentum ℓ, the range of the initial orbital angular momentum depends on the geometry of the detectors in the laboratory frame. In calculations, we carry out summation over the range from ℓ_{min} to ℓ_{max}. The range of ℓ values are specified by the angular acceptance of the detector. In the laboratory frame, the range of the acceptance of the detector is 25°–65°. The range of ℓ values for different geometries are indicated in Table I at $E_{\mathrm{c.m.}} = 502.6$ MeV and Table II at $E_{\mathrm{c.m.}} = 461.9$ MeV. For $E_{\mathrm{c.m.}} = 461.9$ MeV, there are no ℓ values in the side-tip and side-side geometries leading to the acceptance range of the detector. Figure 8 shows cross sections at $E_{\mathrm{c.m.}} = 502.6$ MeV as a function of the mass number A for the production of primary fragments in tip-tip, tip-side, side-tip, and side-side geometries with different colors. To average these cross sections, one must take into account the orientation effects of the deformed nuclei [75,76]. Of course, when only two extreme orientations are considered (side and tip), one needs to define an angle that separates tip and side orientations. In Hinde *et al.* [77], a method was introduced to determine the relative weight between the two orientations, and a critical angle separating the two was found. For the $E_{\mathrm{c.m.}} = 502.6$ MeV cross sections we chose the critical angle to be 37° and averaged as in Refs. [75,76]. The cross sections for the $E_{\mathrm{c.m.}} = 461.9$ MeV case are complicated by the fact that the energy is very close to the Bass barrier of 463.3 MeV, and orientations involving the side geometry are suppressed due to approaching the subbarrier regime. This suggests a further energy dependence of the choice of the critical angle. In this case we chose the critical angle to be 60° to increase the weight of the tip orientation. Figure 9 shows total cross sections at $E_{\mathrm{c.m.}} = 461.9$ MeV energy as a function of the mass number A for the production of primary fragments in tip-tip and tip-side geometries with different colors. Cross sections in side-tip and side-side geometries are nearly zero and are not indicated in the figure. The total cross section is essentially determined by tip-tip and tip-side contributions. Calculations provide good descriptions of measurements that are indicated by yellow triangles for high-energy data and by yellow circles for low-energy data.

Finally, the predictions of primary production cross sections for $N = 126$ isotones in the $^{160}\mathrm{Gd} + {}^{186}\mathrm{W}$ system at $E_{\mathrm{c.m.}} = 502.6$ MeV are given in Fig. 10. It is observed that the primary product cross sections in the tip-side geometry are roughly 1 order of magnitude higher than those in the side-tip and side-side geometries, highlighting the effect of inverse quasifission observed in the tip-side geometry. Results clearly demonstrate that, depending on the deformation and relative orientation of the reaction partners, the outcome of

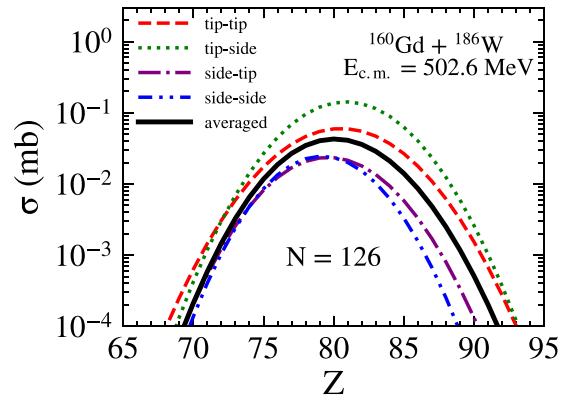

FIG. 10. Primary product cross sections for $N = 126$ isotones in collisions of the $^{160}\mathrm{Gd} + {}^{186}\mathrm{W}$ system at $E_{\mathrm{c.m.}} = 502.6$ MeV are shown as a function of the proton number of the reaction products. Different geometries are indicated by dashed (red), dotted (green), dashed-dotted (purple), and dashed-dot-dot-dashed (blue) lines, whereas the solid black line represents the averaged values.

the reaction differs. This effect supports the idea that MNT reactions can serve as a useful tool to produce neutron-rich heavy nuclei near the lead region, which may not be available via fusion-fission and fragmentation.

V. CONCLUSIONS

We investigate the multinucleon transfer mechanism in quasifission reactions of the $^{160}\mathrm{Gd} + {}^{186}\mathrm{W}$ system at $E_{\mathrm{c.m.}} =$ 502.6 MeV and $E_{\mathrm{c.m.}} = 461.9$ MeV employing the quantal diffusion description based on the stochastic mean-field approach. We evaluate transport coefficients associated with charge and mass asymmetry variables in terms of time-dependent single-particle wave functions of TDHF theory. The transport description includes the quantal effect due to the shell structure, the full geometry of the collision dynamics, and the Pauli exclusion principle and does not involve any adjustable parameters aside from the standard description of the effective Hamiltonian of TDHF theory. In the transport description, in addition to the diffusion coefficient, we need to determine first and second derivatives of the potential energy surface with respect to neutron and proton numbers. It is possible to determine isoscalar and isovector curvature parameters in terms of neutron and proton drift coefficients and diffusion coefficients with the help of Einstein relations. The joint probability distribution of primary fragments is determined by a correlated Gaussian function in terms of mean values of neutron and proton numbers and neutron, proton, and mixed dispersions for each initial angular momentum. We calculate cross sections of primary fragments as a function of mass number and compare with the data of Kozulin *et al.* [53]. Calculations provide good descriptions of primary mass distributions at both bombarding energies.

ACKNOWLEDGMENTS

S.A. gratefully acknowledges Middle East Technical University for warm hospitality extended to him during his visits. S.A. also gratefully acknowledges F. Ayik for continuous support and encouragement. This work is supported in part by U.S. DOE Grants No. DE-SC0015513 and No. DE-SC0013847. This work is supported in part by TUBITAK Grant No. 122F150. The numerical calculations reported in this paper were partially performed at TUBITAK ULAKBIM, High Performance and Grid Computing Center (TRUBA resources).

[1] A. Chatillon, Ch. Theisen, P. T. Greenlees, G. Auger, J. E. Bastin, E. Bouchez, B. Bouriquet, J. M. Casandjian, R. Cee, E. Clément, R. Dayras, G. de France, R. de Toureil, S. Eeckhaudt, A. Göergen, T. Grahn, S. Grévy, K. Hauschild, R.-D. Herzberg, P. J. C. Ikin *et al.*, Spectroscopy and single-particle structure of the odd-Z heavy elements ^{255}Lr, ^{251}Md, and ^{247}Es, Eur. Phys. J. A **30**, 397 (2006).

[2] R.-D. Herzberg, P. T. Greenlees, P. A. Butler, G. D. Jones, M. Venhart, I. G. Darby, S. Eeckhaudt, K. Eskola, T. Grahn, C. Gray-Jones, F. P. Heßberger, P. Jones, R. Julin, S. Juutinen, S. Ketelhut, W. Korten, M. Leino, A.-P. Leppanen, S. Moon, M. Nyman *et al.*, Nuclear isomers in superheavy elements as stepping stones towards the island of stability, Nature (London) **442**, 896 (2006).

[3] E. M. Kozulin, E. Vardaci, G. N. Knyazheva, A. A. Bogachev, S. N. Dmitriev, I. M. Itkis, M. G. Itkis, A. G. Knyazev, T. A. Loktev, K. V. Novikov, E. A. Razinkov, O. V. Rudakov, S. V. Smirnov, W. Trzaska, and V. I. Zagrebaev, Mass distributions of the system $^{136}\mathrm{Xe} + {}^{208}\mathrm{Pb}$ at laboratory energies around the Coulomb barrier: A candidate reaction for the production of neutron-rich nuclei at $N = 126$, Phys. Rev. C **86**, 044611 (2012).

[4] J. V. Kratz, M. Schädel, and H. W. Gäggeler, Reexamining the heavy-ion reactions $^{238}\mathrm{U} + {}^{238}\mathrm{U}$ and $^{238}\mathrm{U} + {}^{248}\mathrm{Cm}$ and actinide production close to the barrier, Phys. Rev. C **88**, 054615 (2013).

[5] Y. X. Watanabe, Y. H. Kim, S. C. Jeong, Y. Hirayama, N. Imai, H. Ishiyama, H. S. Jung, H. Miyatake, S. Choi, J. S. Song, E. Clement, G. de France, A. Navin, M. Rejmund, C. Schmitt, G. Pollarolo, L. Corradi, E. Fioretto, D. Montanari, M. Niikura *et al.*, Pathway for the production of neutron-rich isotopes around the $N = 126$ Shell closure, Phys. Rev. Lett. **115**, 172503 (2015).

[6] V. V. Desai, W. Loveland, K. McCaleb, R. Yanez, G. Lane, S. S. Hota, M. W. Reed, H. Watanabe, S. Zhu, K. Auranen, A. D. Ayangeakaa, M. P. Carpenter, J. P. Greene, F. G. Kondev, D. Seweryniak, R. V. F. Janssens, and P. A. Copp, The $^{136}\mathrm{Xe} + {}^{198}\mathrm{Pt}$ reaction: A test of models of multi-nucleon transfer reactions, Phys. Rev. C **99**, 044604 (2019).

[7] G. G. Adamian, N. V. Antonenko, V. V. Sargsyan, and W. Scheid, Possibility of production of neutron-rich Zn and Ge isotopes in multinucleon transfer reactions at low energies, Phys. Rev. C **81**, 024604 (2010).

[8] G. G. Adamian, N. V. Antonenko, and D. Lacroix, Production of neutron-rich Ca, Sn, and Xe isotopes in transfer-type reactions with radioactive beams, Phys. Rev. C **82**, 064611 (2010).

[9] X. Jiang and N. Wang, Probing the production mechanism of neutron-rich nuclei in multinucleon transfer reactions, Phys. Rev. C **101**, 014604 (2020).

[10] G. G. Adamian, N. V. Antonenko, A. Diaz-Torres, and S. Heinz, How to extend the chart of nuclides? Eur. Phys. J. A **56**, 47 (2020).

[11] S. A. Kalandarov, G. G. Adamian, N. V. Antonenko, H. M. Devaraja, and S. Heinz, Production of neutron deficient isotopes in the multinucleon transfer reaction $^{48}\mathrm{Ca}$ ($E_{\mathrm{lab}} =$ 5.63MeV/nucleon) + $^{248}\mathrm{Cm}$, Phys. Rev. C **102**, 024612 (2020).

[12] C. Li, J. Tian, and F. Zhang, Production mechanism of the neutron-rich nuclei in multinucleon transfer reactions: A reaction time scale analysis in energy dissipation process, Phys. Lett. B, **809**, 135697 (2020).

[13] G. G. Adamian, N. V. Antonenko, H. Lenske, L. A. Malov, and S. Zhou, Self-consistent methods for structure and production of heavy and superheavy nuclei, Eur. Phys. J. A **57**, 89 (2021).

[14] M. G. Itkis, G. N. Knyazheva, I. M. Itkis, and E. M. Kozulin, Experimental investigation of cross sections for the production of heavy and superheavy nuclei, Eur. Phys. J. A **58**, 178 (2022).

[15] S. Heinz and H. M. Devaraja, Nucleosynthesis in multinucleon transfer reactions, Eur. Phys. J. A **58**, 114 (2022).

[16] Z. Wu, L. Guo, Z. Liu, and G. Peng, Production of proton-rich nuclei in the vicinity of ^{100}Sn via multinucleon transfer reactions, Phys. Lett. B **825**, 136886 (2022).

[17] S. Hofmann and G. Münzenberg, The discovery of the heaviest elements, Rev. Mod. Phys. **72**, 733 (2000).

[18] Yu. Ts. Oganessian, V. K. Utyonkov, Yu. V. Lobanov, F. Sh. Abdullin, A. N. Polyakov, R. N. Sagaidak, I. V. Shirokovsky, Yu. S. Tsyganov, A. A. Voinov, G. G. Gulbekian, S. L. Bogomolov, B. N. Gikal, A. N. Mezentsev, S. Iliev, V. G. Subbotin, A. M. Sukhov, K. Subotic, V. I. Zagrebaev, G. K. Vostokin, M. G. Itkis *et al.*, Synthesis of the isotopes of elements 118 and 116 in the ^{249}Cf and ^{245}Cm + ^{48}Ca fusion reactions, Phys. Rev. C **74**, 044602 (2006).

[19] V. I. Zagrebaev, Yu. Ts. Oganessian, M. G. Itkis, and W. Greiner, Superheavy nuclei and quasi-atoms produced in collisions of transuranium ions, Phys. Rev. C **73**, 031602(R) (2006).

[20] V. Zagrebaev and W. Greiner, New way for the production of heavy neutron-rich nuclei, J. Phys. G: Nucl. Part. Phys. **35**, 125103 (2008).

[21] V. Zagrebaev and W. Greiner, Production of new heavy isotopes in low-energy multinucleon transfer reactions, Phys. Rev. Lett. **101**, 122701 (2008).

[22] V. I. Zagrebaev and W. Greiner, Production of heavy and superheavy neutron-rich nuclei in transfer reactions, Phys. Rev. C **83**, 044618 (2011).

[23] A. V. Karpov and V. V. Saiko, Modeling near-barrier collisions of heavy ions based on a Langevin-type approach, Phys. Rev. C **96**, 024618 (2017).

[24] V. V. Saiko and A. V. Karpov, Analysis of multinucleon transfer reactions with spherical and statically deformed nuclei using a Langevin-type approach, Phys. Rev. C **99**, 014613 (2019).

[25] V. Saiko and A. Karpov, Multinucleon transfer as a method for production of new heavy neutron-enriched isotopes of transuranium elements, Eur. Phys. J. A **58**, 41 (2022).

[26] Z.-Q. Feng, G.-M. Jin, J.-Q. Li, and W. Scheid, Production of heavy and superheavy nuclei in massive fusion reactions, Nucl. Phys. A **816**, 33 (2009).

[27] Z.-Q. Feng, G.-M. Jin, and J.-Q. Li, Production of heavy isotopes in transfer reactions by collisions of ^{238}U + ^{238}U, Phys. Rev. C **80**, 067601 (2009).

[28] Z.-Q. Feng, Production of neutron-rich isotopes around $N =$ 126 in multinucleon transfer reactions, Phys. Rev. C **95**, 024615 (2017).

[29] K. Zhao, X. Wu, and Z. Li, Quantum molecular dynamics study of the mass distribution of products in 7.0A MeV ^{238}U + ^{238}U collisions, Phys. Rev. C **80**, 054607 (2009).

[30] K. Zhao, Z. Li, Y. Zhang, N. Wang, Q. Li, C. Shen, Y. Wang, and X. Wu, Production of unknown neutron-rich isotopes in ^{238}U + ^{238}U collisions at near-barrier energy, Phys. Rev. C **94**, 024601 (2016).

[31] N. Wang and L. Guo, New neutron-rich isotope production in ^{154}Sm + ^{160}Gd, Phys. Lett. B **760**, 236 (2016).

[32] C. Simenel, Nuclear quantum many-body dynamics, Eur. Phys. J. A **48**, 152 (2012).

[33] C. Simenel and A. S. Umar, Heavy-ion collisions and fission dynamics with the time-dependent Hartree-Fock theory and its extensions, Prog. Part. Nucl. Phys. **103**, 19 (2018).

[34] T. Nakatsukasa, K. Matsuyanagi, M. Matsuo, and K. Yabana, Time-dependent density-functional description of nuclear dynamics, Rev. Mod. Phys. **88**, 045004 (2016).

[35] V. E. Oberacker, A. S. Umar, and C. Simenel, Dissipative dynamics in quasifission, Phys. Rev. C **90**, 054605 (2014).

[36] A. S. Umar, V. E. Oberacker, and C. Simenel, Shape evolution and collective dynamics of quasifission in the time-dependent Hartree-Fock approach, Phys. Rev. C **92**, 024621 (2015).

[37] A. S. Umar and V. E. Oberacker, Time-dependent HF approach to SHE dynamics, Nucl. Phys. A **944**, 238 (2015).

[38] A. S. Umar, C. Simenel, and W. Ye, Transport properties of isospin asymmetric nuclear matter using the time-dependent Hartree-Fock method, Phys. Rev. C **96**, 024625 (2017).

[39] C. Simenel, Particle transfer reactions with the time-dependent Hartree-Fock theory using a particle number projection technique, Phys. Rev. Lett. **105**, 192701 (2010).

[40] K. Sekizawa and K. Yabana, Time-dependent Hartree-Fock calculations for multinucleon transfer and quasifission processes in the ^{64}Ni + ^{238}U reaction, Phys. Rev. C **93**, 054616 (2016).

[41] K. Sekizawa, TDHF theory and its extensions for the multinucleon transfer reaction: A mini review, Front. Phys. **7**, 20 (2019).

[42] R. Balian and M. Véneroni, Fluctuations in a time-dependent mean-field approach, Phys. Lett. B **136**, 301 (1984).

[43] R. Balian and M. Véneroni, Time-dependent variational principle for the expectation value of an observable: Mean-field applications, Ann. Phys. **164**, 334 (1985).

[44] R. Balian and M. Véneroni, Correlations and fluctuations in static and dynamic mean-field approaches, Ann. Phys. **216**, 351 (1992).

[45] M. Tohyama and A. S. Umar, Quadrupole resonances in unstable oxygen isotopes in time-dependent density-matrix formalism, Phys. Lett. B **549**, 72 (2002).

[46] M. Tohyama, Applications of time-dependent density-matrix approach, Front. Phys. **8**, 67 (2020).

[47] S. Ayik, A stochastic mean-field approach for nuclear dynamics, Phys. Lett. B **658**, 174 (2008).

[48] D. Lacroix and S. Ayik, Stochastic quantum dynamics beyond mean field, Eur. Phys. J. A **50**, 95 (2014).

[49] C. Simenel, Particle-number fluctuations and correlations in transfer reactions obtained using the Balian-Véneroni variational principle, Phys. Rev. Lett. **106**, 112502 (2011).

[50] E. Williams, K. Sekizawa, D. J. Hinde, C. Simenel, M. Dasgupta, I. P. Carter, K. J. Cook, D. Y. Jeung, S. D. McNeil, C. S. Palshetkar, D. C. Rafferty, K. Ramachandran, and A. Wakhle, Exploring zeptosecond quantum equilibration dynamics: From deep-inelastic to fusion-fission outcomes in ^{58}Ni + ^{60}Ni Reactions, Phys. Rev. Lett. **120**, 022501 (2018).

[51] K. Godbey and A. S. Umar, Quasifission dynamics in microscopic theories, Front. Phys. **8**, 40 (2020).

[52] K. Godbey, C. Simenel, and A. S. Umar, Microscopic predictions for the production of neutron-rich nuclei in the reaction ^{176}Yb + ^{176}Yb, Phys. Rev. C **101**, 034602 (2020).

[53] E. M. Kozulin, V. I. Zagrebaev, G. N. Knyazheva, I. M. Itkis, K. V. Novikov, M. G. Itkis, S. N. Dmitriev, I. M. Harca, A. E. Bondarchenko, A. V. Karpov, V. V. Saiko, and E. Vardaci, Inverse quasifission in the reactions ^{156,160}Gd + ^{186}W, Phys. Rev. C **96**, 064621 (2017).

[54] K. Washiyama and D. Lacroix, Energy dissipation in fusion reactions from dynamical mean-field theory, Int. J. Mod. Phys. E **18**, 2114 (2009).

[55] P.-G. Reinhard, A. S. Umar, K. T. R. Davies, M. R. Strayer, and S.-J. Lee, Dissipation and forces in time-dependent Hartree-Fock calculations, Phys. Rev. C **37**, 1026 (1988).

[56] D. J. Kedziora and C. Simenel, New inverse quasifission mechanism to produce neutron-rich transfermium nuclei, Phys. Rev. C **81**, 044613 (2010).

[57] A. S. Umar, M. R. Strayer, J. S. Wu, D. J. Dean, and M. C. Güçlü, Nuclear Hartree-Fock calculations with splines, Phys. Rev. C **44**, 2512 (1991).

[58] A. S. Umar and V. E. Oberacker, Three-dimensional unrestricted time-dependent Hartree-Fock fusion calculations using the full Skyrme interaction, Phys. Rev. C **73**, 054607 (2006).

[59] K.-H. Kim, T. Otsuka, and P. Bonche, Three-dimensional TDHF calculations for reactions of unstable nuclei, J. Phys. G: Nucl. Part. Phys. **23**, 1267 (1997).

[60] S. Ayik, B. Yilmaz, O. Yilmaz, A. S. Umar, and G. Turan, Multinucleon transfer in central collisions of $^{238}\mathrm{U}+{}^{238}\mathrm{U}$, Phys. Rev. C **96**, 024611 (2017).

[61] S. Ayik, B. Yilmaz, O. Yilmaz, and A. S. Umar, Quantal diffusion description of multinucleon transfers in heavy-ion collisions, Phys. Rev. C **97**, 054618 (2018).

[62] B. Yilmaz, S. Ayik, O. Yilmaz, and A. S. Umar, Multinucleon transfer in $^{58}\mathrm{Ni}+{}^{60}\mathrm{Ni}$ and $^{60}\mathrm{Ni}+{}^{60}\mathrm{Ni}$ in a stochastic mean-field approach, Phys. Rev. C **98**, 034604 (2018).

[63] S. Ayik, B. Yilmaz, O. Yilmaz, and A. S. Umar, Quantal diffusion approach for multinucleon transfers in Xe + Pb collisions, Phys. Rev. C **100**, 014609 (2019).

[64] K. Sekizawa and S. Ayik, Quantal diffusion approach for multinucleon transfer processes in the $^{58,64}\mathrm{Ni}+{}^{208}\mathrm{Pb}$ reactions: Toward the production of unknown neutron-rich nuclei, Phys. Rev. C **102**, 014620 (2020).

[65] S. Ayik and K. Sekizawa, Kinetic-energy dissipation and fluctuations in strongly damped heavy-ion collisions within the stochastic mean-field approach, Phys. Rev. C **102**, 064619 (2020).

[66] O. Yilmaz, G. Turan, and B. Yilmaz, Quasi-fission and fusion-fission reactions in $^{48}\mathrm{Ca}+{}^{208}\mathrm{Pb}$ collisions at $E_{\mathrm{c.m.}}=190$ MeV, Eur. Phys. J. A **56**, 37 (2020).

[67] S. Ayik, B. Yilmaz, O. Yilmaz, and A. S. Umar, Merging of transport theory with the time-dependent Hartree-Fock approach: Multinucleon transfer in U + U collisions, Phys. Rev. C **102**, 024619 (2020).

[68] S. Ayik, M. Arik, O. Yilmaz, B. Yilmaz, and A. S. Umar, Multinucleon transfer mechanism in $^{250}\mathrm{Cf}+{}^{232}\mathrm{Th}$ collisions using the quantal transport description based on the stochastic mean-field approach, Phys. Rev. C **107**, 014609 (2023).

[69] C. W. Gardiner, *Quantum Noise* (Springer-Verlag, Berlin, 1991).

[70] U. Weiss, *Quantum Dissipative Systems*, 2nd ed. (World Scientific, Singapore, 1999).

[71] H. Risken and T. Frank, *The Fokker–Planck Equation* (Springer-Verlag, Berlin, 1996).

[72] G. Scamps and C. Simenel, Impact of pear-shaped fission fragments on mass-asymmetric fission in actinides, Nature (London) **564**, 382 (2018).

[73] S. Ayik, O. Yilmaz, B. Yilmaz, and A. S. Umar, Heavy-isotope production in $^{136}\mathrm{Xe}+{}^{208}\mathrm{Pb}$ collisions at $E_{\mathrm{c.m.}}=514$ MeV, Phys. Rev. C **100**, 044614 (2019).

[74] W. U. Schröder, J. R. Huizenga, and J. Randrup, Correlated mass and charge transport induced by statistical nucleon exchange in damped nuclear reactions, Phys. Lett. B **98**, 355 (1981).

[75] K. Godbey, A. S. Umar, and C. Simenel, Deformed shell effects in $^{48}\mathrm{Ca}+{}^{249}\mathrm{Bk}$ quasifission fragments, Phys. Rev. C **100**, 024610 (2019).

[76] A. S. Umar and V. E. Oberacker, $^{64}\mathrm{Ni}+{}^{64}\mathrm{Ni}$ fusion reaction calculated with the density-constrained time-dependent Hartree-Fock formalism, Phys. Rev. C **77**, 064605 (2008).

[77] D. J. Hinde, M. Dasgupta, J. R. Leigh, J. C. Mein, C. R. Morton, J. O. Newton, and H. Timmers, Conclusive evidence for the influence of nuclear orientation on quasifission, Phys. Rev. C **53**, 1290 (1996).